Journal of
Materials Chemistry A

ROYAL SOCIETY
OF CHEMISTRY

PAPER

View Article Online
View Journal | View Issue

Cite this: *J. Mater. Chem. A*, 2025, **13**, 38301

Surface-enhanced and electric field-modulated reactivity of Fe(IV)═O complexes: unveiling the synergy of Lewis acid additives, Au(111), and graphene surfaces in biomimetic C–H activation

Rupesh Kumar Tiwari,† Asmita Sen,† Sourav Mondal
and Gopalan Rajaraman*

Achieving high reactivity and maintaining selectivity simultaneously is one of the holy grails of catalytic transformations; while metalloenzymes perform this task effortlessly, synthetic models that mimic their reactivity often struggle to achieve either of the goals set. High-valent $\mathrm{Fe^{IV}{=}O}$ species are highly reactive oxidants, but their elevated activity often limits catalytic turnover due to rapid catalyst degradation and over-oxidation of substrates. To overcome these shortcomings, here we have explored electrostatic and surface effects in tuning the reactivity of $[(\mathrm{F_8})\mathrm{Fe^{IV}(O)}]$ (**1**) and $[(\mathrm{F_8})\mathrm{Fe^{IV}(O)}](\mathrm{LutH})^+$ (**2**) using density functional theory (DFT) and periodic DFT calculations. To begin with, the effect of Lewis acid ($\mathrm{LutH^+}$ 2,6-lutidinium triflate) is explored, which is found to induce a local electric field and diminishes the kinetic barrier by ~15 kJ mol^{-1}. As the addition of adducts and their direct role in the oxidation process are difficult to control, we explored the possibility of employing oriented external electric fields (OEEFs) to gain control over the reactivity and the oxidation process. Our results demonstrate that applying an OEEF along the $\overset{\ominus\longrightarrow\oplus}{\mathrm{Fe{=}O}}$ direction reduces the kinetic barrier further by ~29 kJ mol^{-1}, while along the $\overset{\oplus\longleftarrow\ominus}{\mathrm{Fe{=}O}}$ direction, proton transfer was preferred, offering an intriguing way to channelise selectivity. Surface interactions provide additional control: Au(111) lowers the barrier by ~58 kJ mol^{-1} under OEEFs, whereas graphene inhibits reactivity, requiring an OEEF along the +*Z*-direction to reduce the barrier by ~49 kJ mol^{-1}. By integrating chemical modifications and external control, this study offers a general framework for designing next-generation oxidation catalysts across diverse catalytic systems.

Received 5th May 2025
Accepted 29th September 2025

DOI: 10.1039/d5ta03554f

rsc.li/materials-a

1. Introduction

Electrostatic catalysis deals with the modification of chemical reactions with electric fields and is commonly employed by enzymes to perform various transformations.[1–3] In enzymatic reactions, the less polar active side binds a substrate in a precisely aligned direction and the charged residues within the enzyme sites create a local electric field (LEF) to facilitate the catalytic activity – the reason behind their superior performance compared to biomimetic models.[4–6] Here, a local electric field refers to the electrostatic field generated by charged or polar residues within an enzyme's active site. It precisely orients and polarises the substrate to stabilise the transition state and enhance catalytic efficiency. For instance, a large intramolecular electrostatic field in the active site is found to be operative in stabilising the various intermediates and lowering the intrinsic reaction barriers as well in cytochrome P450 enzymes and other related heme metalloenzymes.[7–12] Furthermore, mutation of a single residue Phe429 to histidine results in the deactivation of cytochrome P450 (CYP) and a closer analysis reveals that the FeO–OH bond undergoes heterolysis in the presence of Phe429 and generates highly reactive $\mathrm{Fe^{V}{=}O}$ species, while histidine facilitates homolysis of the same bond leading to $\mathrm{Fe^{IV}{=}O}$ species that do not have aggressive oxidizing ability to activate inert C–H bonds.[9]

Efforts have been made in recent years to capture this missing piece to improve the catalytic reactivity of biomimetic models.[13–16] This has been achieved to some extent by introducing charged functional groups on the substrate or the catalysts.[17,18] This was demonstrated in the work of Groves and co-workers, who reported two charge-coronated complexes $[\mathrm{por^{\bullet+}Fe^{IV}(O)L_{ax}}]$ and $[\mathrm{PyPzFe^{III}(OH)L_{ax}}]$, which were analogues to Cpd I of cytochrome P450 enzymes.[19,20] The rate of hydrogen abstraction by these biomimetic models was significantly higher compared to their conventional uncharged counterparts.[21] This rate enhancement, therefore, was attributed to the

---

Department of Chemistry, Indian Institute of Technology Bombay, Powai, Mumbai – 400076, India. E-mail: rajaraman@chem.iitb.ac.in

† Rupesh and Asmita contributed equally to this manuscript.

generation of a local electric field due to the presence of charged functional groups in the porphyrin ring. As all chemical reactions are associated with the movement of electrons, these are expected to be influenced by the application of external electric fields.[22] It is demonstrated that applying an electric field can stabilise charged-separated resonance contributors, which in turn stabilise chemical species that otherwise are not stable. Therefore, electrostatic effects can rouse the ionicity of a bond that undergoes dissociation or new bond formation and stabilise the corresponding transition state, reducing the overall kinetic barrier. Shaik and co-workers established the use of the oriented external electric field (OEEF) as a tool to enhance/retard the rate of a chemical reaction using computational methods.[22,23] Here, an OEEF is a deliberately applied electric field with a fixed direction and magnitude that interacts with a molecular system. It can modulate the electronic structure, stabilise specific states, and influence reaction pathways or catalytic activity. For example, Shaik and co-workers argued that OEEFs can introduce significant ionicity in homonuclear bonds such as H–H and Li–Li along the *Z*-direction (the bond axis). The degree of ionic character that arises depends on the strength of the applied field and molecular polarizability. Any covalent bond of the X–Y type can be viewed as the combination of several resonance contributors like [X–Y ↔ X + Y− ↔ X − Y+].[24,25] In a certain electric field, these charged contributors are found to be stabilised, which in turn stabilises a structure. In the absence of an external electric field, the relative electronegativities of X and Y atoms control the extent of either of the charge-separated contributors to resonance stabilisation of the bond. The extent of contributions from the charge-separated structures is controlled by the direction of the applied electric field and molecular polarizability. In another study, they demonstrated that the application of OEEFs is found to affect the regioselectivity of hydroxylation *vs.* epoxidation during the reaction of a high-valent $\mathrm{Fe^{IV}{=}O}$ dependent porphyrin radical cation (Cpd I) with propene as a substrate. It was observed that a positive field ($F_z > 0$) along the S–Fe–O direction prefers hydroxylation, while a negative field ($F_z > 0$) along the S–Fe–O direction prefers epoxidation.[23] Furthermore, on the organometallic front, the rate of oxidative addition of aryl/alkyl electrophiles and CO_2 reduction can be regulated by the application of an external electric field along the reaction axis associated with electron reorganisation.[26,27] The use of OEEFs is found to regulate the extent of charge transfer in the transition state. It is found that even in a small applied OEEF of 0.26 V $\mathrm{\AA^{-1}}$, the mechanism for the oxidative addition in aryl halides (Ph–X) changes to a nucleophilic aromatic substitution $\mathrm{CS_N}$Ar process, while in the absence of a field, it is a concerted oxidative addition.[27]

Recently, Coote and co-workers provided experimental support to this approach by studying a C–C bond formation in a Diels–Alder reaction, where it was shown that the application of an electric field in a particular direction enhanced the reactivity and selectivity.[17] After this pioneering experimental validation, the utilisation of OEEFs or designed local electric fields (D-LEFs) to boost the reactivity has gained the attention of both experimentalists and theoreticians.[28] The role of electrostatic interactions in modulating product selectivity is also found in other examples, such as in metalloenzymes. Halogenation overriding hydroxylation is attributed to various charge–dipole interactions and induced electric field effects originating from charged amino acid residues.[29] This work has provided novel insights into the role of the globular part of the protein in reactivity, suggesting that the introduction of such effects is indispensable for biomimetic models striving to surpass enzymatic reactions. However, the incorporation of these interactions is challenging in the biomimetic model and in this direction, the work of Karlin and co-workers on the synthesis and reactivity of a heme $\mathrm{Fe^{IV}{=}O}$ complex $[(F_8)\mathrm{Fe^{IV}(O)}]$ (**1**) (here F_8 = tetrakis(2,6-difluorophenyl)porphyrinate) and $[(F_8)\mathrm{Fe^{IV}(O)}](\mathrm{LutH})^+$ (**2**) (here $\mathrm{LutH^+}$ = 2,6-lutidinium triflate) (Fig. 1a and b) assumes relevance. In this set of complexes studied, protic Lewis acid $\mathrm{LutH^+}$ was introduced in the secondary coordination sphere in **2** to assess the role of such Lewis acid in catalysis.[30,31] It was found that **2** reacts 40 times faster than **1** for the C–H bond activation of xanthene, and **1** is found to be unreactive to the substrate with a higher bond-dissociation energy, such as DHA.

While the presence of a Lewis acid may explain the observed reactivity differences, the combination of a cationic acid with strongly fluorinated ligands and the oxyl oxygen atom in **2** likely generates a significant permanent dipole. This dipole can effectively mimic a local electric field (LEF), suggesting an alternative, non-covalent route to modulate reactivity. Motivated by this insight, we systematically investigated the LEF effects on the reactivity of complex **1**, employing a range of oriented external electric fields (OEEFs) to evaluate whether this non-chemical approach could replicate the catalytic efficiency observed in complex **2**.

Unlike earlier studies by Coote and co-workers, who experimentally applied electric fields *via* scanning tunnelling microscope (STM) tips to modulate Diels–Alder reactions (Scheme 1a),[17] and Shaik and co-workers, who computationally demonstrated OEEF effects on similar reactions using DFT (Scheme 1b),[32] our work is the first to combine biomimetic high-valent $\mathrm{Fe(IV){=}O}$ chemistry with surface immobilization and OEEF modulation. We extend the field by fabricating complex **1** on realistic surfaces (Au(111) and graphene) to emulate the physical environment of the STM setup (Scheme 1c–e), thereby providing an unprecedented surface-bound, field-directed catalytic model for oxidative transformations. This integrative strategy—merging biomimetic design, surface chemistry, and electric-field-based control—represents a significant advance over previous isolated approaches and opens new directions for electrically tunable catalysis.[33–36]

The models studied here give the opportunity to not only explore the effect of surface interactions on spin-states during C–H activation, but also, for the first time, explore the effect of OEEFs in the catalysis of a high-valent paramagnetic $\mathrm{Fe^{IV}{=}O}$ system on various surfaces. With this, we aim to answer the following intriguing questions: (i) how does the designed LEF influence reactivity, and can this effect be replicated through the application of an OEEF? (ii) How can modelling suitable surfaces, such as Au(111) and graphene, modulate catalytic

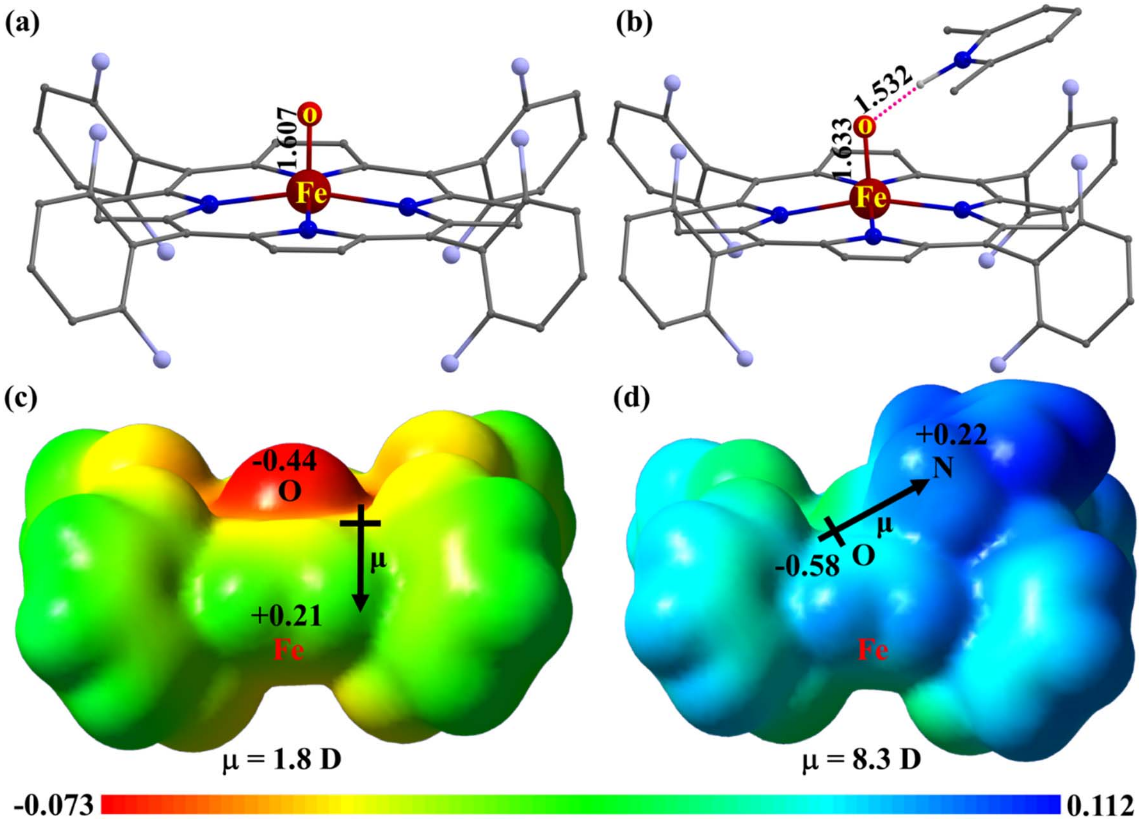

Fig. 1 Ground state ($S = 1$) DFT optimized structure of (a) **1** and (b) **2** with selected structural parameters. (c) and (d) The electrostatic potential map of complexes **1** and **2** in the $S = 1$ state. Colour code: Fe, deep red; O, light red; N, blue; F, light blue; C, grey. Hydrogen atoms are omitted for clarity. Red and blue regions in the ESP map represent areas of negative and positive potential, respectively, with numbers corresponding to their magnitude in kJ mol^{-1}. Bond lengths are in Å. The black arrow shows the dipole moment direction.

activity through their interactions with the catalyst? (iii) Can an OEEF enhance the reactivity of surface-adsorbed catalysts, providing high-throughput insights for C–H activation?

2. Results

Electronic structure of 1 and 2

Both **1** and **2** (Fig. 1a and b) possess a triplet ground state ($S = 1$), with the quintet $S = 2$ state lying at 34.3 kJ mol^{-1} and 5.3 kJ mol^{-1}, respectively (Fig. S1). The $S = 0$ singlet state lies at considerably higher energy >100.0 kJ mol^{-1} in both cases, eliminating their role in further reaction mechanisms. Another spin-state corresponding to an Fe^{III}–O$^{\bullet}$ structure ($S = 3$) is possible, which is significantly high-lying (89.9 kJ mol^{-1}) in **1** while it lies at 22.3 kJ mol^{-1} in **2** (Fig. S1). The predicted ground state is consistent with the spectral data reported from the experiments and also based on the earlier DFT calculations on similar complexes.[30,37,38] The DFT calculated Fe–O bond lengths of 1.607 Å and 1.633 Å for **1** and **2** at the ground state are consistent with the experimental data, where a slight elongation in the Fe–O bond is observed upon addition of an acidic group. The computed ν(Fe=O) of 833 cm^{-1} and 811 cm^{-1} is also consistent with the experimentally reported resonance Raman data reported for **1** and **2** (833 and 819 cm^{-1}), respectively, offering confidence in the methodology chosen.[30] X-ray absorption fine structure spectroscopy (XAFS) reveals a short 1.65 Å Fe–O bond in horseradish peroxidase compound **I**, which is well fitted with our DFT computed Fe–O bond length in **1** and **2**. A similar Fe–O bond length is further observed in chloroperoxidase compound **I**. These metalloenzymes are reported to have a formal Fe–O double bond in their active site. This indicates the presence of an Fe–O double bond in **1** and **2** even after protonation. This is in line with the experimental observation where **2** was identified as a Lewis acid adduct rather than a fully protonated Fe–OH species.

The addition of LutH$^+$ to **1** resulted in a significant drop in the quintet–triplet energy gap (ΔE_{QT}) in **2** (Fig. S1). A closer look at the $S = 2$ geometry of **2** reveals that the proton of LutH$^+$ is fully transferred to the oxo group, leading to the formation of a protonated Fe^{III}–O species with an additional electron coming from the F_8 ligand, which is reflected in the computed eigenvalue and spin density plot of **2** (Fig. 2 and S2). A significant spin-up (α) electron density is developed on the F_8 ligand at the $S = 2$ state of **2**, while no such behaviour is noted for **1**. Thus, the quintet state of **2** has a tautomeric structure of [($F_8^{\bullet+}$)Fe^{III}(O)⋯H(Lut)], which is an artificial analogue of protonated Cpd-II, [(Por)Fe^{IV}(OH)] species. It was also suggested previously that [(Por$^{\bullet+}$)FeIII–OH] exists during the desaturation pathway of P450$_{cam}$.[39] Additionally, there are reports of square-pyramidal [($F_8^{\bullet+}$)Fe^{III}(OH)] species exhibiting very high reactivity with the

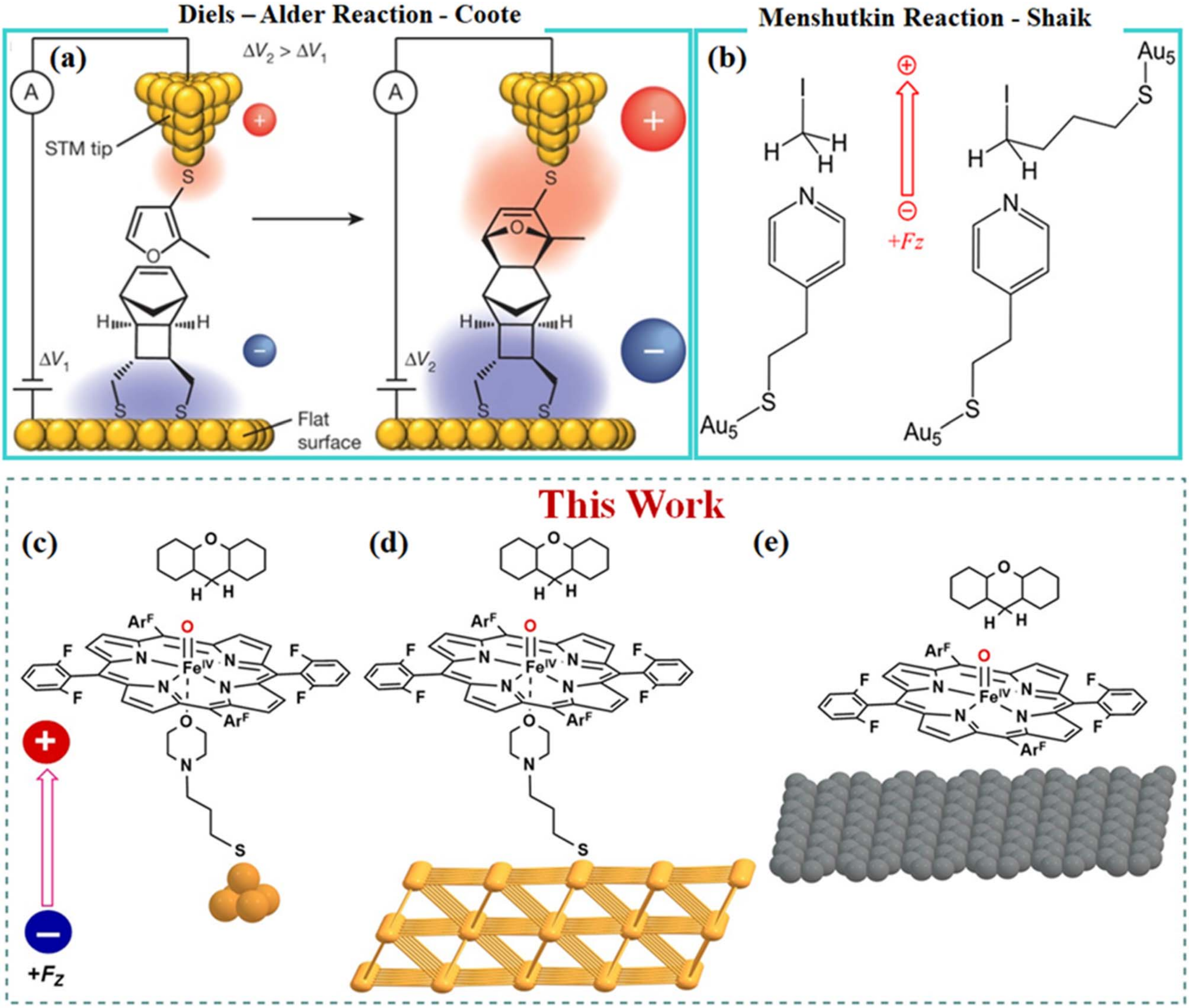

Scheme 1 (a) Schematic description of the catalysis of a Diels–Alder reaction affected by a bias voltage between a gold STM tip and a gold surface.[17] (b) Models used to study the interplay of the OEEF and gold thiol linkers' effect on the Menshutkin reaction.[18] (c)–(e) C–H bond activation of xanthene by complex **1** with the Au_5 STM tip, the gold surface and graphene respectively mimicking the experimental set-up with the effect of OEEFs.

measured rate constants resembling that of the reported rate constant value of **2**, offering confidence in the established tautomeric form in the quintet state.[40] Furthermore, the elongation of the Fe–O bond in **2** leads to stabilisation of the d_{z^2} orbital compared to **1** by 5.2 eV, contributing to the substantial reduction of ΔE_{QT} observed in **2**.

The computed UV-Vis spectra of the ground and first excited state of **1** (Fig. S3a) are similar (416 nm *vs.* 402 nm and 564 nm *vs.* 593 nm for triplet *vs.* quintet states), and these agree well with the experimental features observed at 415 nm and 544 nm measured at −90 °C (Fig. S3b). However, for complex **2**, calculations predict a broad shoulder in the 750–1000 nm region for the quintet state, which is absent for the triplet state (Fig. S4a). This unique feature originates due to the charge transfer from the Fe–(F_8) bonding orbital to the $\pi^*(F_8^{\bullet+})$ antibonding orbital. The absorption spectra of complex **2**, as observed experimentally, clearly indicate the presence of unique near-infrared bands (700–1000 nm, Fig. S4b). These bands strongly support the presence of reduced species, which is consistent with the outcomes predicted from our calculations. Calculations reveal a similar dipole moment (μ) of 1.8 D and 1.9 D in $S = 2$ and $S = 1$ spin states of **1**, respectively, while the addition of $LutH^+$ develops a significant difference in the dipoles in $S = 2$ (2.3 D) and $S = 1$ (8.3 D) spin states (Table S2). Moreover, the direction of μ is along the Fe–O bond in both spin-states of **1**, while the direction has shifted along the $(LutH^+)$–O direction in the triplet state of **2**. In the $S = 2$ state of **2**, μ is parallel to the $Fe(F_8)$ plane. These observations emphasise the difference in the intricate electronic structure of these species *i.e.*, $[(F_8)Fe^{III}(O)\cdots H(Lut)]$ and $[(F_8^{\bullet+})Fe^{III}(O)\cdots H(Lut)]$ species in the $S = 1$ and $S = 2$ spin states in **2**. The electrostatic potential (ESP) map generated for the triplet state of **1** and **2** (Fig. 1c and d)

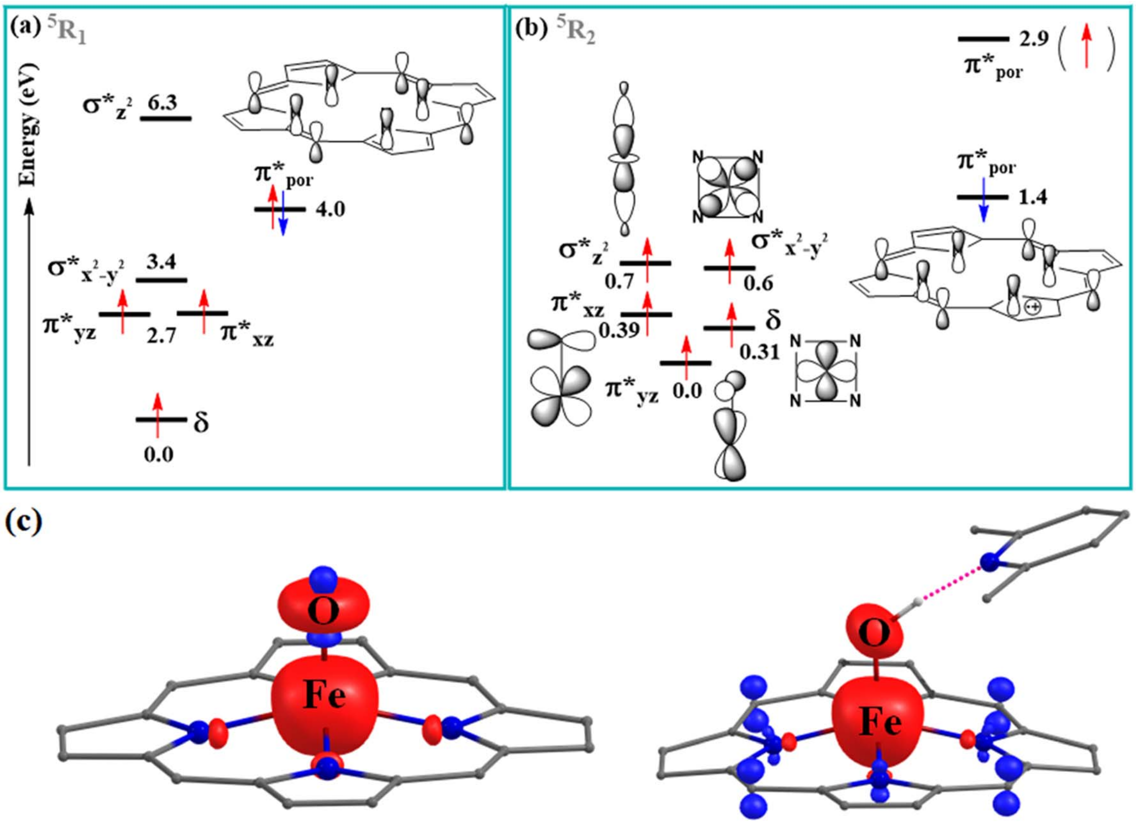

Fig. 2 Key orbitals associated with canonical molecular orbitals in (a) $^5R_1$ and (b) $^5R_2$ along with their (c) spin population respectively: $^5R_1$, left side and $^5R_2$, right side. α spin-up and β spin-down are denoted as red and blue surfaces. The isosurface value is ±0.03 au. The colour codes for Fe, C, N, O, and H atoms are set as deep red, grey, blue, red and white respectively.

unambiguously reveals a large variation in the charge distribution, and therefore, one can expect their behaviour under an electric field to be drastically different from one another.

C–H bond activation by 1 and 2

To understand the reactivity of **1** and **2**, we have considered their reaction with xanthene. Both were found to react with xanthane, producing xanthone as a major product with estimated rate constants of 0.369 M^{-1} S^{-1} and 14.2 M^{-1} S^{-1}, respectively. Experimentally, the first C–H bond activation step is determined to be the rate-limiting step, and therefore, the mechanism shown in Fig. 3a and b is adapted for our calculations. The estimated barrier height for **1** (**2**) at the triplet and quintet surfaces is found to be 72.4 kJ mol^{-1} (75.1 kJ mol^{-1}) and 65.3 kJ mol^{-1} (50.2 kJ mol^{-1}), respectively (Fig. 3c and d). This suggests that C–H bond activation occurs at the quintet surface for both complexes, following the conventional two-state reactivity.[41] While the Fe–O bond distance in the $S = 2$ state is slightly elongated in the case of **1** (1.626 Å) compared to the ground state, it is significantly longer in **2** (1.757 Å) due to the Fe^{III}–OH nature of this species. At the $^5TS_2$, this bond further elongates to 1.749 Å and 1.829 Å for **1** and **2**, respectively. It is important to note here that the Fe–O distance of 1.829 Å in $^5TS_2$ resembles the general Fe–O distance of 1.820 Å in the Cpd II of P450,[42] suggesting that it mimics Cpd II, rationalising also the higher reactivity observed. On the rate-limiting $S = 2$ surfaces, the C–H bond activation process in **1** (**2**) is associated with the transfer of an α-electron to the metal centre (porphyrin), leaving behind a β-spin on the substrate, indicating a concerted hydrogen atom transfer mechanism. In **2**, an α-electron is transferred to the π* orbital of the porphyrin moiety, which is expected to enhance the overall exchange-enhanced reactivity (EER),[43] leading to a reduction in the barrier height. After the transition state, the formation of the intermediate is assumed, and its formation is found to be exothermic for both species. However, for **2**, this is found to be significantly larger compared to **1** (−87.1 *vs.* −33.4 kJ mol^{-1}) for $^5INT_1$ and $^5INT_2$. The larger stabilisation found for $^5INT_2$ is associated with the formation of Fe^{III}–OH_2 species *vis-à-vis* Fe^{III}–OH species. The formation of Fe^{III}–OH_2 is detected in the experiments using Mössbauer and EPR measurements and supports the mechanistic findings.[30] To probe whether the higher reactivity of **2** compared to **1** towards the C–H bond is electrostatic in nature, we have quantified the amount of the LEF exerted by the $LutH^+$ dangling near the Fe^{IV}=O moiety using the TITAN code.[44] The net LEF in **1** is estimated to be 0.68 V $Å^{-1}$ at the reactive oxyl centre directed along the Fe → O axis on the $S = 2$ surfaces. However, in **2**, on the same spin state, the calculated net field is increased to 4.66 V $Å^{-1}$ at the same oxyl centre. The higher reactivity of **2**, therefore, can be attributed to the very high LEF generated on the

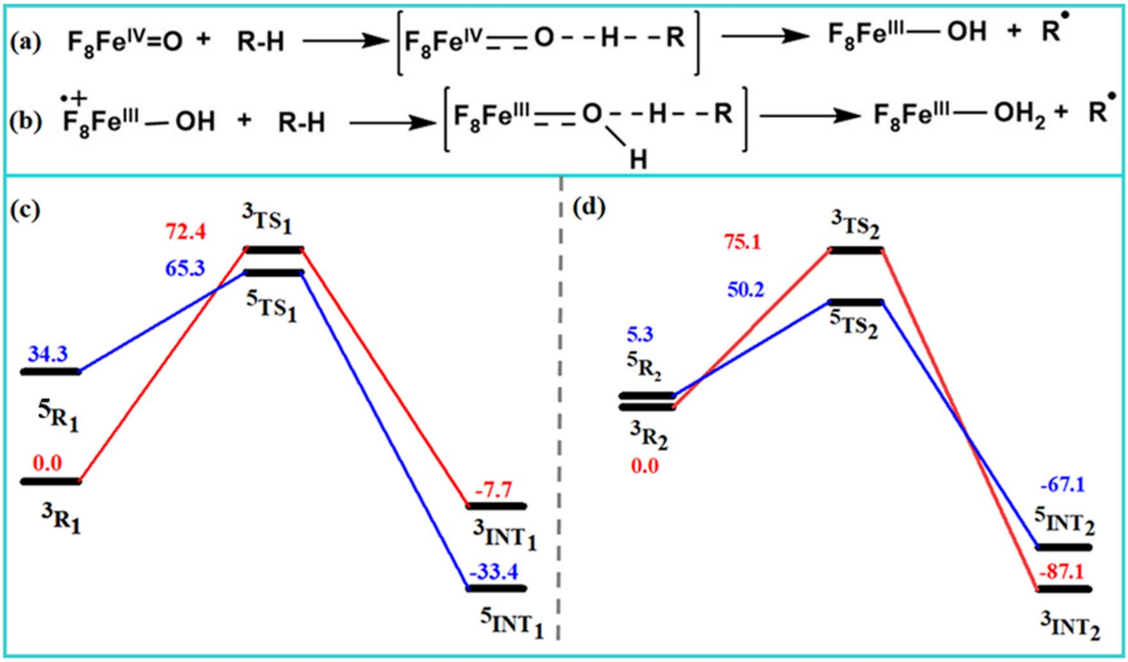

Fig. 3 Schematic representation of C–H bond activation of xanthene by (a) **1** and (b) **2**, along with the corresponding potential energy surfaces (c) and (d), respectively. Energies are in kJ mol^{-1}.

oxygen, which increases the basicity of the corresponding iron-oxo/hydroxo species, facilitating the facile concerted hydrogen atom transfer mechanism. At the $S = 1$ surface, as expected, a reverse scenario is observed, while the reduced LEF of 0.96 V Å^{-1} in **2** as compared to 1.83 V Å^{-1} in **1** can be correlated with the higher C–H activation barrier of the former (75.1 kJ mol^{-1} *vs.* 72.4 kJ mol^{-1}), indicating that the modulation of LEF values can be considered a promising tool to enhance/retard the reactivity of Fe^{IV}/Fe^{III}–O(OH) species.

For catalyst **1**, the rate-limiting step produces the xanthenyl radical and [F$_8$Fe^{III}OH], followed by a rebound step in which the radical is hydroxylated to form [F$_8$Fe^{III}OH(xanthene)]. This intermediate readily dissociates to xanthene hydrol, which is oxidised by two equivalents of **1** to yield xanthone. In the rebound transition state, spin-state analysis indicates that $S = 1$ is the ground state while $S = 2$ remains at 15.0 kJ mol^{-1} higher in energy. The other spin state, such as $S = 3$, lies 47 kJ mol^{-1} higher in energy. The $S = 3$ surface can therefore be excluded from the transition state. The rebound step features very low activation barriers—7.6 kJ mol^{-1} ($S = 1$) and 4.3 kJ mol^{-1} ($S = 2$)—with Fe–O distances of 1.808 Å and 1.839 Å, respectively, at the transition states.

Electric field effects on the reactivity of 1

The aforementioned section illustrates how the introduction of a cationic moiety (LutH^{+}) can trigger the reactivity of an Fe^{IV}═O species by introducing a greater LEF around the catalytic centre, hence, in turn, reducing the hydrogen abstraction barrier in **2**. The observed prominence of the LEF in lowering the barrier height suggests that externally applying an electric field has the potential, in principle, to emulate the characteristics of the lutidinium cation and even diminish the barrier height further. To test this hypothesis, we systematically investigated the reactivity of complex **1** towards the C–H bond activation of xanthene under the influence of OEEFs applied along the Fe═O bond axis (defined as the *Z*-axis) in the range of -45×10^{-4} au to $+45 \times 10^{-4}$ au.[21,45] It is found that the absolute energy of both the triplet and quintet states decreases irrespective of the direction of the applied field, while the gap between the quintet and triplet states remains consistent. The drop-in energy is in the range of 1–7 kJ mol^{-1} until a $+15 \times 10^{-4}$ au field, and it decreases sharply for larger fields (>15.0 kJ mol^{-1}) in the +*Z*-direction ($\overset{\ominus}{\mathrm{Fe}}\overset{\longrightarrow}{=\!=}\overset{\oplus}{\mathrm{O}}$) (Fig. 4a), accompanied by a larger increase in the spin density on the quintet (triplet) state of Fe, reaching up to 3.451 (1.345) at $+45 \times 10^{-4}$ au. Conversely, in the opposite direction ($\overset{\oplus}{\mathrm{Fe}}\overset{\longleftarrow}{=\!=}\overset{\ominus}{\mathrm{O}}$), a similar gradual decrease is observed, with spin densities of 3.376 and 1.288 at -45×10^{-4} au for $S = 2$ and $S = 1$ spin states, respectively. This is mirrored by a concomitant decrease (increase) in the spin density on the F$_8$ porphyrin moiety, indicating ligand-to-metal charge transfer and the emergence of an [F$_8$$^{\bullet+}$Fe^{III}] resonance character under the applied field (Table S3 and Fig. 4a inset).

Interestingly, under a positive OEEF, the Fe–O bond (Table S4) elongates, promoting the polarisation of charge, with Fe becoming more electropositive and the oxyl oxygen becoming more negative—clearly seen in the electrostatic potential (ESP) map, where the oxygen site appears prominently red (Fig. S5). This charge separation enhances the dipole moment, which reaches 9.1 D for the $S = 2$ state at $+45 \times 10^{-4}$ au. Conversely, when the field is applied in the opposite ($-Z$) direction, the Fe–O bond shortens, yet the dipole moment still increases (up to

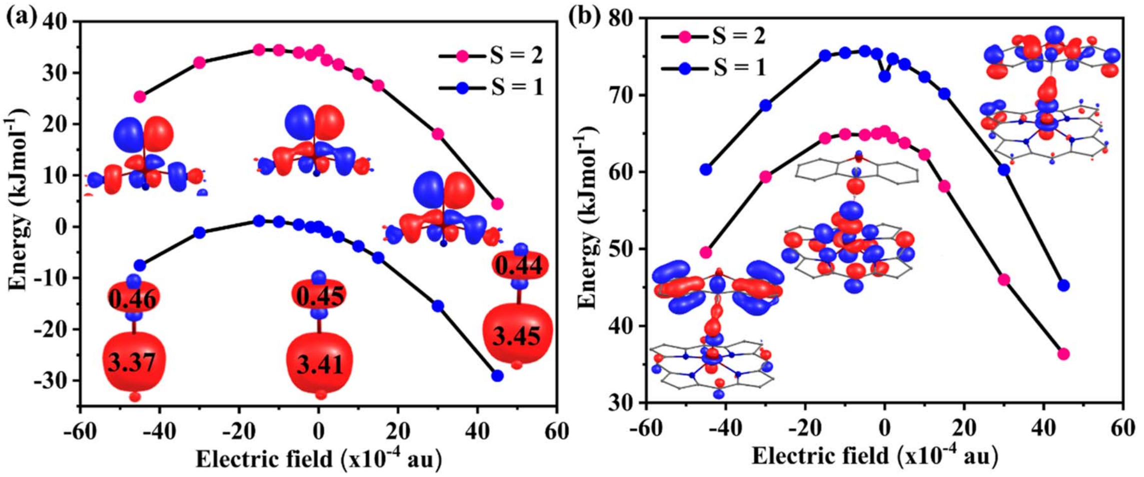

Fig. 4 DFT computed quintet–triplet energy gap (kJ mol^{-1}) of **1** (a) in R and (b) in the TS in the absence and presence of OEEFs varying from -45×10^{-4} au to $+45 \times 10^{-4}$ au.

4.7 D), driven by a reversed but still significant polarisation (Table S4).

From a molecular orbital perspective, the d_{z^2} orbital of Fe is stabilised by 0.3 eV in the $+Z$ direction, whereas the energy of the porphyrin-centred orbital remains unchanged (at ∼4.0 eV from the ground d_{xy} orbital; Fig. S6 and S7). Conversely, in the negative direction, the gap initially increases as the d_{z^2} orbital is destabilised. However, at larger field strengths, this increase tends to saturate, limiting the ΔE ($E_{\sigma_{\text{C–H}}} - E_{d_{z^2}}$; Fig. S8) gap. This is also clearly witnessed in the HOMO of the transition state, with a very little overlap between the $\sigma_{\text{C–H}}$ and d_{z^2} orbitals (Fig. 4b inset). This orbital reorganisation stabilises distinct electronic configurations in both triplet and quintet spin surfaces, which modulates the Fe=O oxidising strength.

To assess how these changes affect reactivity, we calculated the C–H bond activation transition states under applied fields. As shown in Fig. 4b, the activation barrier decreases symmetrically in both directions of the OEEF, forming a parabolic dependence similar to that observed for the triplet and quintet state energies. While small fields induced minimal changes (few kJ mol^{-1}), strong fields yielded a substantial barrier drop—from 65.0 kJ mol^{-1} under the zero field to 36.3 kJ mol^{-1} at $+45 \times 10^{-4}$ au and ∼49 kJ mol^{-1} at -45×10^{-4} au ($S = 2$ surface). This symmetric barrier reduction, despite an asymmetric Fe–O bond length change, arises from distinct electronic modification in both field directions.

In the $+Z$ direction, a decrease in the transition barrier is noted due to the following reasons: (i) the donor ($\sigma_{\text{C–H}}$) and acceptor (d_{z^2}) orbital energy gap monotonically decreases with increasing field strength. At high fields, the d_{z^2} orbital is sufficiently stabilised to facilitate effective electron transfer from the $\sigma_{\text{C–H}}$, enhancing the hydrogen atom transfer (HAT) efficiency. (ii) As the field increases, the spin density on Fe in the transition state ($^5TS_1$) increases gradually (from 3.859 to 3.876), accompanied by reduced spin on the porphyrin, indicating enhanced ligand-to-metal electron donation and a growing $[(F_8^{\bullet +})Fe^{III}{=}O]$ resonance character. Additionally, an increase in oxo spin density (*e.g.*, −0.175 at $+10 \times 10^{-4}$ au; Table S6) suggests greater oxo basicity, which facilitates more efficient HAT. The Fe–O bond also elongates at the transition state, reinforcing this reactive configuration (Table S7). (iii) Careful observation of singly occupied spin natural orbitals (SNOs) in $^5TS_1$ in the absence and the presence of OEEFs ($+45 \times 10^{-4}$ au) indicates that the first four singly occupied orbitals are Fe 3d(π^*) orbitals. The next is a mixture of $\sigma^*_{\text{Fe}} + \pi_{\text{O}}$ bonding orbitals with an occupancy of 0.61 and 0.74 in the zero field and at $+45 \times 10^{-4}$ au field, respectively. The beta counterpart is a combination of $\pi_{\text{F8}} + \pi_{\text{sub}} + \pi_{\text{O}}$ orbitals. In the presence of an electric field, the occupancy of $\pi_{\text{F8}} + \pi_{\text{sub}} + \pi_{\text{O}}$ orbitals is found to be higher, indicating a better involvement of the F_8 moiety (Fig. S9–S11).

In the $-Z$-direction, an overall decrease in the transition barrier at higher fields is witnessed due to (i) a significant reduction of spin localisation on the substrate at the transition state, indicating a mechanistic shift from HAT to proton transfer followed by the electron transfer (PTET) mechanism. (ii) A negligible occupancy (0.15) of the δ orbitals agrees with the stepwise PTET mechanism (Fig. S9–S11). (iii) At a higher field, the energy gap between the donor ($\sigma_{\text{C–H}}$) and acceptor (d_{z^2}) orbital saturates while the dipole moment increases due to enhancement in the polarisation.

Similar to the rate-limiting step, the application of the field along the Fe=O axis completely removes the transition barrier for the rebound step, irrespective of the field direction. For both the $S = 1$ and $S = 3$ spin states, the finite zero-field barriers of 7.6 kJ mol^{-1} and 4.3 kJ mol^{-1}, respectively, vanish under applied fields of $\pm 45 \times 10^{-4}$ a.u., rendering the process barrierless.

The critical role of gold clusters and the thiolate linker in facilitating C–H bond activation

To replicate an experimental setup analogous to that employed in the initial investigation of electrostatic catalysis in the Diels–Alder reaction by Coote and co-workers,[17] complex **1** was immobilized on an $Au_{216}(111)$ surface *via* a tethering group

$\{(O(CH_2CH_2)_2N)(CH_2)_3S\}$ positioned at the vacant axial site (Fig. S12a) and DFT optimization was performed. The use of a larger morpholine alkylthio ligand $\{(O(CH_2CH_2)_2N)(CH_2)_3S\}$ for fabricating the catalyst on the surface aims to minimise spin and geometric alterations around the active Fe metal center of the catalyst after adsorption onto the surface. Prior investigations into heterogeneous catalysis have highlighted the role of gold clusters.[17,18] Furthermore, the involvement of multiple spin states in **1** introduces additional complexity. The substantial computational demands associated with these large systems cannot be overlooked. The most straightforward strategy to address this complexity is to adopt the approach outlined earlier,[17,18] which involves substituting the large Au(111) cluster with a simplified model consisting of a gold tip (Au_5; Fig. 5a). Additionally, the stability of complex **1** on various gold surfaces was evaluated using models of different sizes: a large model (Au_{216}), a medium model (Au_{48}), and a small model (Au_5 tip; Fig. S12). The binding energies (∼−254 kJ mol^{-1}, Table S8)

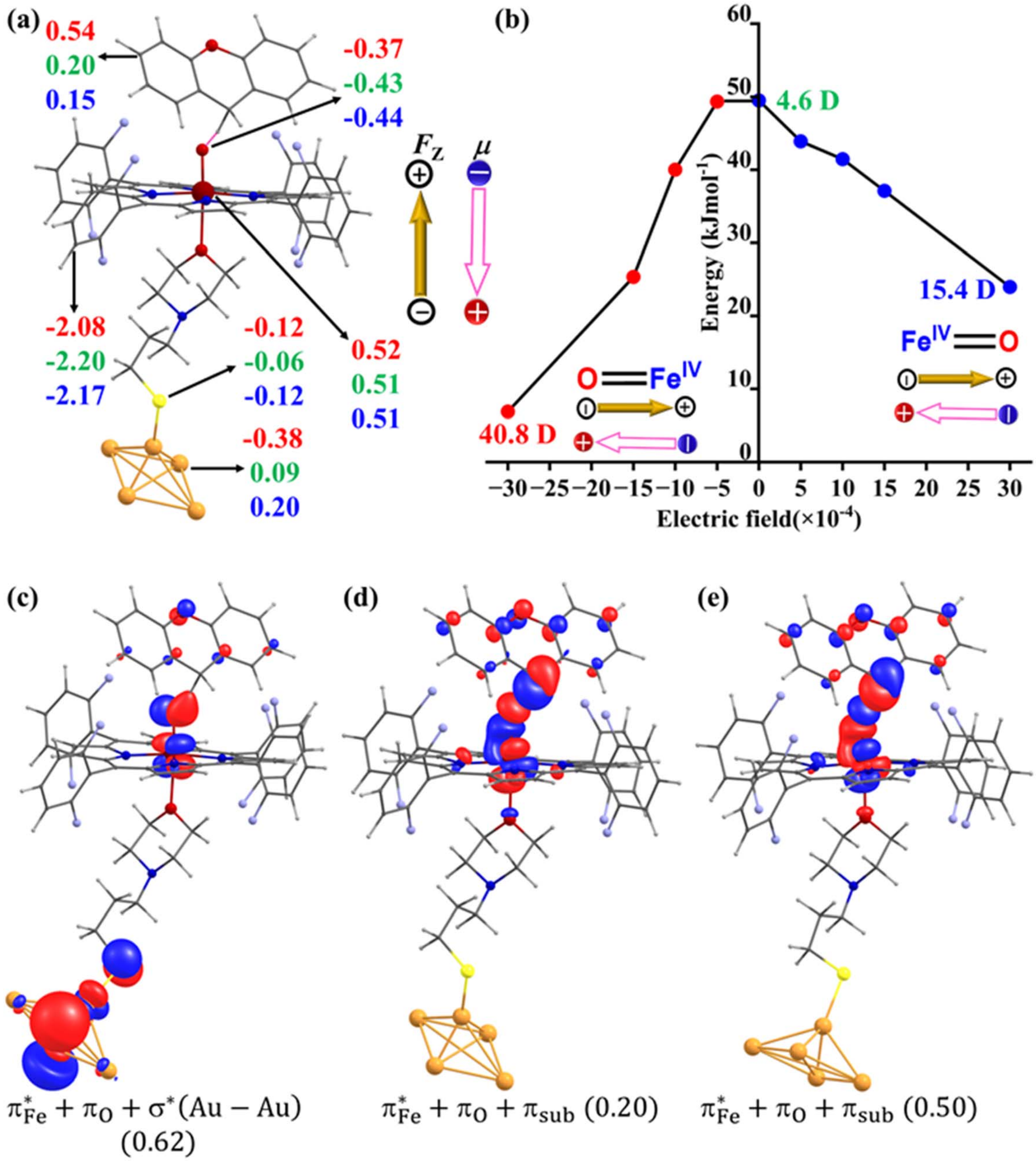

Fig. 5 (a) NPA calculated natural charges on the C–H bond activation transition state by **3** at the $S = 1$ spin state. (b) The C–H bond activation barrier in the absence and presence of OEEFs varies from -30×10^{-4} au to $+30 \times 10^{-4}$ au. The changes in the overall dipole moment at the transition states are shown at $F_z = 0$ and $F_z = \pm 30 \times 10^{-4}$ au. The colour codes for the charges are green in the absence of an OEEF and red and blue for $F_z = -30 \times 10^{-4}$ au and $+30 \times 10^{-4}$ au, respectively. The arrow in yellow and pink shows the convention of $+F_z$ and the overall dipole moment direction. Spin natural orbitals of $^3TS_3$ at (c) $F_z = -30 \times 10^{-4}$ au, (d) $F_z = 0$, and (e) $F_z = +30 \times 10^{-4}$ au. The SNO composition and occupancy (in parentheses) are shown at the bottom.

indicated similar stability across all models, regardless of the number of gold atoms incorporated, corroborating earlier reports.[46–48] This consistency arises because the primary molecule-surface interaction—namely, the Au⋯S bond—remains unchanged across the models where the Au atoms have the same coordination environment, ensuring that the essential interfacial electronic features are well-represented even with a smaller cluster. Calculations reveal that the geometries computed with large, medium, and small models are similar to each other and consistent with an $S = 1$ ground state, with the $S = 2$ remaining at around 45 kJ mol^{-1} higher in energy, eliminating the possibility of the $S = 2$ spin state participating in the reaction mechanism. A similar manifestation in geometry and spin state energetics of **1** on these models led us to continue the rest of the calculations employing an Au$_5$ tip. In the final model, complex **1** was anchored to an Au$_5$ tip *via* an (O(CH$_2$CH$_2$)$_2$-N)(CH$_2$)$_3$S-linker (hereafter referred to as **3**), enabling the substrate to interact freely with the catalyst while being subjected to a bias voltage. The computed bond parameters and spin density values (Tables S9 and S10) reflect that when **1**, in the $S = 2$ states, is tethered through the Au$_5$ tip, it gets converted to $S = 1$ at the metal centre, showing a very strong spin delocalisation from the catalyst to the Au(111) surface. The stabilisation of the low-spin state of Fe$^{\mathrm{II/III/IV}}$-containing systems after grafting on an Au(111) surface was previously reported by several groups.[49–51] The C–H bond activation barrier in **3** reduces to 49.5 kJ mol^{-1}, indicating that the Au$_5$ STM tip acts as a co-catalyst. The energies of the canonical orbitals in ^{3}TS$_3$ show a better matching in energy between the low-lying σ(C–H) and $\pi^*_{yx/xz}$ orbitals (both lie at 1.3 eV), which facilitates β-electron transfer to the metal and, therefore, lowers the intrinsic energy barrier for this step.

The intrinsic C–H activation barrier of xanthene as a function of the OEEF applied along the Fe–O axis in **3**, ranging from -30×10^{-4} au to $+30 \times 10^{-4}$ au, is depicted in Fig. 5b. Similar to **1**, the application of OEEFs in **3** along the +*Z*-direction leads to the enhancement in the Fe–O bond length and in spin density on the Fe metal site (Tables S11 and S12). A reverse scenario is observed in the opposite direction. Reaction energetics reveals that the intrinsic C–H activation barrier gradually decreases as the field is applied in the +*Z*-direction (along the Fe–O direction, blue region). As we reverse the direction of the electric field (along the O–Fe direction), the C–H activation barrier decreases slowly, like in the +*Z*-direction. However, the energy barrier reduces abruptly beyond -15×10^{-4} au and reaches as low as 6.8 kJ mol^{-1} at a field value of -30×10^{-4} au (Fig. 5b). For both **1** and **3**, the hydrogen abstraction barrier tends to decrease with the application of an electric field irrespective of the direction; however, the scenario is reversed in **1**, where the blue curve bends more steeply than the red curve. What leads to the improved catalytic behaviour of **3** with the implication of OEEFs in both ±*Z*-directions? During the application of OEEFs in the +*Z*-direction, augmentation of natural charge is observed on the Au$_5$ moiety, indicating the participation of the Au$_5$ cluster during the hydrogen atom transfer transition state (Table S13). The increased dipole moment of −15.4 D in ^{3}TS$_3$ [$Z + (30 \times 10^{-4})$] as compared to the −4.6 D in ^{3}TS$_3$ (zero-field) supports the above observation. The reversing of the OEEFs to the −*Z*-direction (along the Fe–O direction) results in a flow of electron density from the substrate to the Au$_5$ cluster, depleting the natural charges to −0.383 on the Au$_5$ moiety with a concomitant increase on xanthene. This is well supported by the change in the dipole moment value for the entire system from 15.4 D to 40.8 D (Table S14). The significant enhancement of dipole moment values in the transition states with OEEFs both in the ±*Z*-direction increases the ionic character of the Fe–O bond and, therefore, facilitates the C–H bond activation process. Although the natural charges and associated dipole moments explain the catalytic behaviour of **3** in Fig. 5, the understanding of the electronic structure is pivotal. The first two sets of SNOs of ^{3}TS$_3$ in the zero-field and the presence of OEEFs in the +*Z*-direction are located on two Fe 3d(π*) orbitals, and the other set is a bonding $\pi^*_{\mathrm{Fe}} + \pi_{\mathrm{O}}$ orbital in an antibonding combination with the σ(C–H) orbital. The occupancy of the latter SNOs is low, which is 0.20 and 0.50, respectively. When the direction of the electric field flips, the second set of SNO transforms into an antibonding $\pi^*_{\mathrm{Fe}} + \pi_{\mathrm{O}} + \sigma^*_{(\mathrm{Au-Au})}$ orbital, with a spin-up α occupancy of 0.62. Its spin-down β-counterpart has σ*(C–H) character. Therefore, with a negative electric field of $-(15\text{–}30) \times 10^{-4}$ au, the Au$_5$ cluster becomes active and acts as an open-shell singlet state and facilitates the C–H bond activation process (Fig. 5c–e).

The effect of the graphene surface on the reactivity of 1

To investigate the influence of the graphene surface on the catalytic reactivity of **1**, we constructed a graphene supercell comprising 192 carbon atoms and grafted **1** onto it. Thereafter, a periodic DFT optimisation was performed to investigate the stable orientation of complex **1** on the graphene surface. The catalyst is stabilised on the graphene surface through a parallel orientation of its porphyrin ring, maximising π⋯π and C–H⋯π non-covalent interactions (hereafter referred to as **1**||@graphene). Additionally, the fluorine substituents in **1** orient toward the graphene surface, further enhancing stability *via* C–F⋯π interaction (Fig. S13).[52–55] The strong stabilisation of **1** on graphene is supported by a binding energy of −236 kJ mol^{-1}, indicating a significant interaction between the molecule and the substrate. This adsorption mechanism is further confirmed by the broadening of hydrogen (H) and fluorine (F) peaks in the projected density of states (pDOS), along with a shift to lower energy levels in the valence band due to C–H⋯π and C–F⋯π interactions. Additionally, a redistribution of carbon (C) peaks is observed, attributed to π⋯π interactions (Fig. S14).

To capture the effect of the graphene surface and OEEF together, the peripheral carbons were capped with hydrogen atoms to create a cluster model of graphene, and the OEEF was applied in a direction perpendicular to the graphene surface. **1**||@graphene preferentially stabilises in the $S = 1$ spin state, with Fe metal possessing a spin density of 1.364 (^{3}**1**||@graphene). Similar to model **3**, when **1**||@graphene is optimised in $S = 2$ states (^{5}**1**||@graphene), it is found that the Fe metal centre remains in the $S = 1$ configuration with a spin density of around 1.364, while the remaining two unpaired electrons were found on the hydrogen-passivated edge carbon atoms of the graphene substrate (Fig. S16). $^5\mathbf{1}\|$@graphene is found to be slightly less stable than the $S = 1$ spin state and remains at 15.3 kJ mol^{-1} higher in energy. The presence of $S = 1$ at the Fe site in $^5\mathbf{1}\|$@graphene is also supported by the pDOS of Fe, O and N atoms of **1** before and after the adsorption at the graphene surface. It is found that on going from $^5R_1$ to $^5\mathbf{1}\|$@graphene, one of the α e_g peaks of Fe gets transferred to the β t_{2g} in the valence band (VB) and, therefore, an increase in the β t_{2g} peak is noted in the VB while an increase in the α peak is noted in the conduction band (CB). Also, the peaks of the O atom shift towards the CB, which further suggests a decrease in the spin density of the O atom (Fig. 6a and b). Although $^5\mathbf{1}\|$@graphene is slightly destabilised as compared to $^3\mathbf{1}\|$@graphene, the C–H bond activation barrier with the prior case is significantly low, which is 74.5 kJ mol^{-1}, compared to the 134.5 kJ mol^{-1} with $^3\mathbf{1}\|$@graphene (Fig. S15). The physisorption of **1** on the graphene surface, therefore, increases the C–H bond activation barrier as compared to the free complex **1** by 9.2 kJ mol^{-1}. In both spin states, the Fe metal is in the triplet state; the only difference lies with the electronic involvement of the graphene with the free catalyst, indicating that the involvement of the graphene is required to maintain the catalytic reactivity of **1** when adsorbed on a surface. Furthermore, we carefully checked the strength of C–H⋯π, C–F⋯π and π⋯π noncovalent interactions, which are found to be stronger in $^5\mathbf{1}\|$@graphene. A shorter porphyrin–graphene surface distance (~0.1 Å) in the $S = 2$ spin state than in the $S = 1$ facilitates more stable fabrication of the catalyst on the graphene surface with larger reactivity.

After the catalyst immobilisation, the effect of OEEFs was studied further. Similar to the aforementioned systems, we have applied OEEFs perpendicular to the surface, *i.e.*, along the Fe–O bond of the catalyst and an increase in the Fe–O bond length is noted when applied along the +*Z*-direction (Table S15). However, considering the large size of this system and the related computational cost, we have limited our calculations to exploring the effect of OEEFs in fewer electric field values. Similar to model **3**, with the OEEFs, the C–H activation barrier decreases steadily, irrespective of the direction of the application. However, the sensitivity of the activation energy is found to

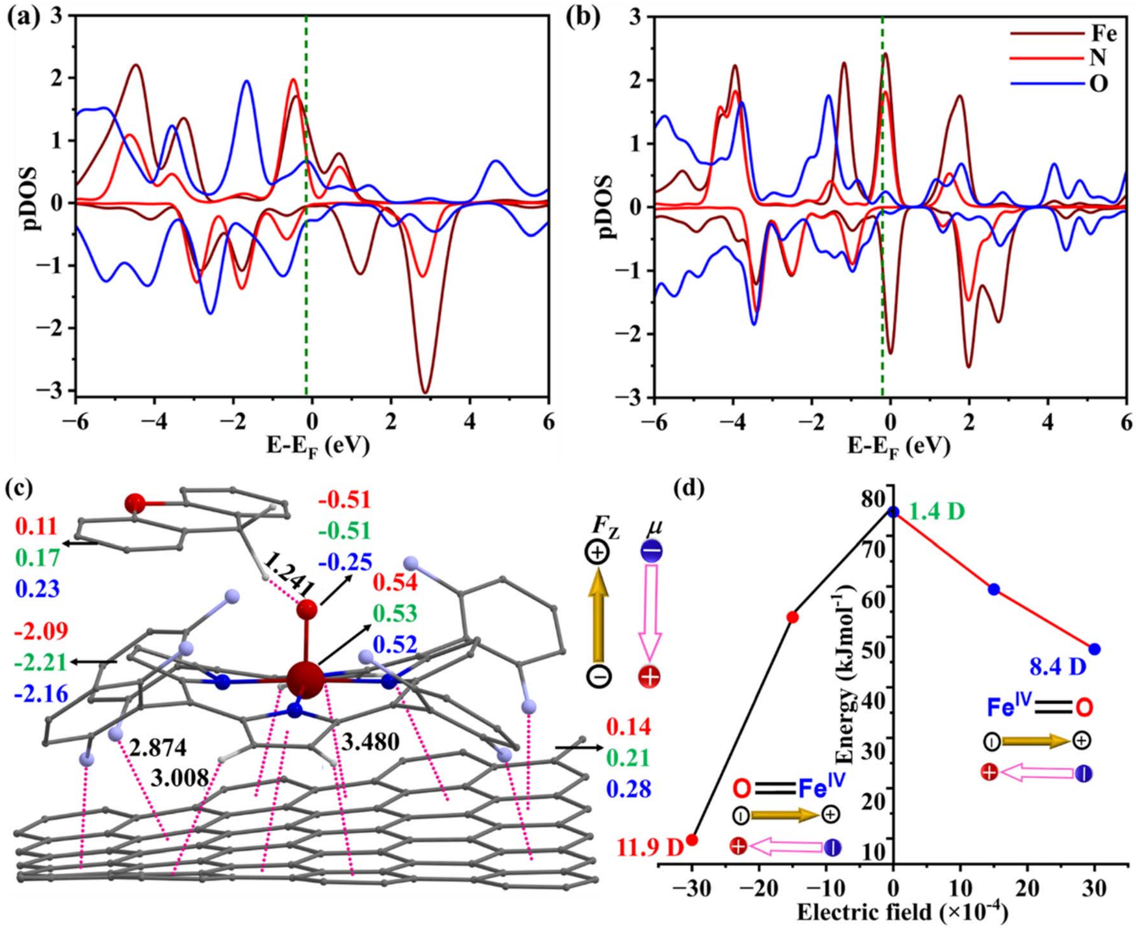

Fig. 6 (a) and (b) pDOS of **1** ($S = 2$) in pristine form and after the deposition at the graphene surface, respectively. (c) NPA calculated natural charges on the C–H bond activation transition state catalysed by $^5\mathbf{1}\|$@graphene. The pink dotted line shows the non-covalent interaction. (d) The C–H bond activation barrier in the absence and presence of OEEFs varies from -30×10^{-4} au to $+30 \times 10^{-4}$ au. The changes in the overall dipole moment at the transition states are shown at $F_z = 0$, and $F_z = \pm 30 \times 10^{-4}$ au. The colour codes for the charges are green in the absence of an OEEF and red and blue for $F_z = -30 \times 10^{-4}$ au and $+30 \times 10^{-4}$ au, respectively. The arrow in yellow and pink shows the convention of $+F_z$ and the overall dipole moment direction.

be drastically higher in the $-Z$-direction, where the energy barrier reduces to 9.7 kJ mol^{-1} with a 30×10^{-4} au field (Fig. 6c and d). Application of an OEEF of 30×10^{-4} au along the $-Z$-direction results in a flow of negative charge from the oxyferryl moiety to the graphene during the hydrogen abstraction process, accumulating a greater negative charge on the graphene by 0.067 units as compared to the zero field (Table S16), while along the $+Z$ direction, a reverse scenario is observed, resulting in the reduction of negative charge by 0.068 units on graphene. However, in both cases, the overall dipole moment in the transition states is increasing, having values of 8.5 D and 11.9 D, respectively, in both $+Z$ and $-Z$-directions. At the zero-field, the dipole moment is found to be significantly low, 1.456 D (Table S17). A careful investigation of the SNOs associated with the lowest energy transition state at 30×10^{-4} au field along the $-Z$-direction shows five sets of singly occupied α natural orbitals. Among them, three are located at the Fe 3d(π^*) orbitals and two are located at the π_{graphene} orbital. Another SNO with an occupancy of 0.33 is found to be located as bonding $3d\pi^*_{\text{Fe}} + \pi_{\text{O}}$ with an antibonding combination with the π_{sub} orbital. In the beta part, one SNO is found to be located on the Fe–O unit and another one is found on graphene. This indicates the greater involvement of graphene during the C–H bond activation process (Fig. S16) when the field is applied along the $-Z$ direction.

3. Discussion

Harnessing protic source-induced electric fields as a co-catalyst

The electronic structure of **1** is more like that of Cpd II, having an [(F_8)Fe^{IV}(O)] formalism. In contrast, **2** can be better described as one electron-reduced Cpd I, better expressed as [($F_8{}^{\bullet+}$)Fe^{III}(O)···H(Lut)]. In the presence of a Lewis acid, an electron is transferred from the porphyrin moiety to the metal–oxo part of the molecule, increasing the overall polarity and increasing the local electric field in **2**. The experimentally detected higher reduction potential of **2** ($+0.46 < E_{1/2} < +0.695$ V) as compared to **1** ($-0.53 < E_{1/2} < -0.43$ V) *vs.* Fc$^{+/0}$ can be directly correlated to the greater local electric field on the oxyl centre due to the presence of LutH$^+$ in **2**. Therefore, the introduction of a protic source to the active site of the metal is used to strategically increase the local electric field, which is inversely proportional to the hydrogen abstraction energy barrier. This effect suggests that externally applying an oriented electric field can emulate the impact of chemical modifications and aid in reducing the barrier.

Harnessing oriented external electric fields as a co-catalyst

In a quest to understand the effect of OEEFs in a paramagnetic Fe^{IV}=O catalyst during C–H bond activation, it is noticed that the reaction energy barrier reduces irrespective of the field direction. Structural illustration indicates a gradual development of [Fe^{III}($F_8{}^{\bullet+}$)] character introduced when $F_z > 0$, therefore mimicking the structural characteristics induced by LutH$^+$ in **2**. This enhances the polarity during the free catalyst and in the C–H bond activation transition state as well, therefore, increasing the overall dipole moment in the respective species and assisting in lowering the energy barrier for the proton-coupled electron transfer reaction. At $F_z < 0$, a reverse flow of electrons enhances the Fe^{IV}=O covalent character, which in turn increases the oxyl radical centre and basicity in the species, which promotes a basicity-driven different PT-ET mechanism.

Harnessing surface-enhanced electric fields as a co-catalyst

The effect of an external electric field on the activation energy barrier becomes highly sensitive when **1** is attached to an Au(111) or graphene surface, as the surface directly modifies the electronic structure and reactivity. If the OEEFs are applied, energy barriers were found to be lower in both $\pm Z$-directions; however, with the introduction of the surface, the extent of reduction in the barrier height is larger at $F_z < 0$, particularly beyond 15×10^{-4} au. During the C–H bond activation process, charge transfer occurs from the substrate to the Au_5 cluster or graphene surface, enhancing the ionic character of the Fe–O bond and increasing the overall dipole moment. This charge redistribution contributes to the reduction of the activation energy barrier. When the direction of the external electric field is reversed, a corresponding reversal in charge flow is observed. The enhanced reactivity of the system can be attributed to the non-innocent nature of these surfaces, which play a critical role in facilitating the catalytic process. These findings emphasise the dual role of the gold/graphene surfaces and OEEFs in optimising electronic and geometric parameters for efficient catalysis, providing insights for future catalyst designs incorporating nanoscale gold/graphene surfaces and external electric fields.

Harnessing external electric fields for enhanced catalysis

While a Lewis acid cation aids in lowering the C–H activation barrier by 15 kJ mol^{-1}, the electrostatic effect imposed by the external electric field is significantly stronger, which helps in lowering the energy barrier by 28.9 kJ mol^{-1} at an OEEF of 45×10^{-4} au.[31,56] This indicates that the catalytic reactions are more sensitive towards an induced electrostatic effect in a non-chemical way rather than a chemical modification. Moreover, the sensitivity of the catalytic transformation to the external electric field is markedly enhanced when the catalyst is anchored to a non-innocent surface. This enhancement is observed regardless of the nature of the catalyst–surface interaction, whether through chemisorption on Au(111) or physisorption on a graphene surface. Notably, the energy barrier is drastically reduced by more than 55 kJ mol^{-1}, even under a lower applied electric field.

Contrasting catalytic roles of graphene and Au(111) surfaces in C–H activation

The C–H bond activation barrier for xanthene using pristine complex **1** is calculated to be 65 kJ mol^{-1}. This barrier is modulated upon surface adsorption, and it decreases to 49.5 kJ mol^{-1} when adsorbed on the Au(111) surface, while it increases to 74.5 kJ mol^{-1} when adsorbed on graphene. The cocatalytic behaviour of the Au(111) surface is due to the following reasons: (i) charge transfer from Au(111) to complex **1** is noted, which increases the oxyl basicity and hence its H-abstraction tendency. (ii) A better energy alignment between the low-lying σ_{C-H} orbital and the $\pi^*_{yx/xz}$ orbital (both located around 1.3 eV) facilitates β-electron transfer to the metal center, thereby lowering the intrinsic activation barrier. (iii) A significant increase in the overall dipole moment (1.8 D in catalyst **1** to 3.8 D in catalyst **3**) and spin density (0.44 in catalyst **1** to 0.81 in catalyst **3**) is noted when **1** is adsorbed on Au(111), which results in reducing the overall activation barrier. When complex **1** is adsorbed on graphene, the following are noted: (i) there is charge transfer from complex **1** to graphene as suggested by the Mulliken charge analysis, and adsorption is supported through weak non-covalent C–H$\cdots\pi$, C–F$\cdots\pi$ and $\pi\cdots\pi$ interactions. (ii) The pDOS analysis suggests that there is a transfer of O-peak from the valence band to the conduction band after the adsorption. (iii) A decrease in the overall dipole moment at the transition state (1.4 D) and a larger energy gap between the low-lying σ_{C-H} and the $\pi^*_{yx/xz}$ orbitals are noted. This synergic effect leads to an increase in the C–H activation barrier when **1** is adsorbed on the graphene surface.

4. Conclusions

The study reveals key insights into the electronic structures and reactivities of complexes **1** and **2**, both of which possess a triplet ($S = 1$) ground state. While the quintet ($S = 2$) state is higher in energy for both complexes, the addition of $LutH^+$ to **1** significantly reduces the quintet–triplet energy gap in **2**, altering its electronic structure and reactivity. The addition of $LutH^+$ to **1** forms a tautomeric $[(F_8^{\bullet+})Fe^{III}(O)\cdots H(Lut)]$ species in **2**, which mirrors the protonated compound **II** found in metalloenzymes and explains its enhanced catalytic activity.

Complex **2** exhibits significantly higher reactivity for the xanthane substrate, and this enhanced reactivity is attributed to the higher local electric field (LEF) generated by the $LutH^+$ in **2** at the oxyl centre, which increases the basicity of the oxo group and facilitates the bond activation process. In contrast, **1** exhibits a lower LEF and, consequently, lower reactivity. Applying a positive field (+*Z*) elongates the Fe–O bond, enhances Fe spin density, and strengthens donor–acceptor interactions, lowering the quintet-state barrier to 36.3 kJ mol^{-1} at +45 × 10^{-4} au from 65.0 kJ mol^{-1} in the field-free state. In contrast, a negative field (−*Z*) destabilises the d_{z^2} orbital, shifts the mechanism toward a proton-transfer pathway *via* an Fe^{III}–O intermediate and modulates bond distances, spin densities, and ∠Fe–O–H angles, highlighting the OEEF as a powerful tool for catalytic optimisation.

Grafting complex **1** onto Au(111) *via* thiolate linkers stabilises its $S = 1$ spin state, enhances C–H activation, and drastically lowers reaction barriers. Strong covalent interactions and spin delocalisation restrict spin-state accessibility, favouring direct reactivity. A gold cluster model facilitates π-channel interactions, reducing the activation barrier to 49.5 kJ mol^{-1}, while an applied OEEF enables a near-barrierless reaction—dropping to just 6.8 kJ mol^{-1} at −30 × 10^{-4} au. This unprecedented synergy between Au(111) and the OEEF offers a powerful strategy for catalytic control, unlocking ultrafast reactivity beyond conventional tuning methods.

Grafting complex **1** onto graphene stabilises the $S = 1$ spin state *via* $\pi\cdots\pi$, C–H$\cdots\pi$, and C–F$\cdots\pi$ interactions, while the $S = 2$ state forms a charge-transfer species $[(\text{graphene})^{\bullet-}(Fe^{IV}{=}O)]$ with comparable reactivity. Under positive OEEFs, the triplet-state C–H activation barrier plummets to 16.7 kJ mol^{-1} at +45 × 10^{-4} au, while the quintet state remains unaffected. Negative OEEFs raise the triplet-state barrier, demonstrating precise tunability. This reveals graphene and OEEFs as potent tools for spin-state control, unlocking new pathways to enhance Cmpd-II catalyst reactivity and opening a new way to heterogeneous catalysis using high-valent $Fe^{IV}{=}O$ species.

5. Computational details

All the density functional theory calculations were carried out using the Gaussian 16 (Revision C.01) suite.[57] The geometries of all stationary points were optimised without any restrictions using the unrestricted B3LYP hybrid density functional[58] along with a double-ξ quality LanL2DZ basis set with Los Alamos effective core potential[59] for metal (Fe) and a 6-31G* basis set for the rest of the atoms, such as H, C, O, N, and F. The choice of the functional is based on the previous literature and the available related benchmarking.[21,60,61] We have also performed a few benchmark calculations using other functionals—PBE,[62] B97-1,[63] TPSSh,[64] B3LYP*[65,66] and PBE0 (ref. 67)—which span a range of Hartree–Fock exchange from 0% to 25%. These benchmarks focus on the $S = 1$ and $S = 2$ spin-state energy gap in complex **2**. Experimental data indicate that $S = 1$ is the ground state, with $S = 2$ lying slightly higher in energy. Our B3LYP calculation reproduces this well, predicting a gap of 5.3 kJ mol^{-1}, while the other functionals show larger deviations. This supports the continued use of B3LYP as the most accurate functional for this system (see Table S18). To ensure that the selected parameters and computed energetics are well-optimised, we performed SCF convergence tests in Gaussian using several convergence criteria. The results were found to be consistent across the methods (see Table S19). Harmonic vibrational frequency calculations have been performed to characterise the nature of all stationary points. Dispersion correction to the optimised geometry and computed energetics is incorporated using the EmpiricalDispersion = GD3 keyword.[68] All global minima are identified by all positive frequencies, while the transition states are indicated by a single imaginary frequency. Intrinsic reaction coordinate (IRC) calculations were performed at the same level to verify that the transition states connect the minima on either side of the saddle point. The energies were refined by the single-point calculations on the DFT optimised structures at the same level of theory using an all-electron Def2-TZVPP basis set.[69] The effect of solvation has been incorporated by employing the SMD solvation model using tetrahydrofuran as a solvent. The final energies presented in the manuscript and ESI are solvation and free energy incorporating enthalpic and entropic contributions at 298.15 K.

The net local electric field strength on Fe and the oxo-ligand in the Fe–O moiety imposed by $LutH^+$ and the peripheral functional groups is quantified by using the TITAN code developed by Shaik and co-workers.[44] The effect of a finite electric field has been incorporated into the calculations using the "Field = M ± N" keyword available in Gaussian 16. The notation defines the axis of the OEEF (M), its direction (±), and magnitude (N) in au. The strength of the electric field has varied between -45×10^{-4} and $+45 \times 10^{-4}$ au (where 1 au = 51.4 V $Å^{-1}$) in all systems studied. The electric field is oriented along the *Z*-axis, which is the Fe–O bond direction, as the substrate approaches the catalyst. At first, complete geometry optimisation of various reactants, intermediates, and transition states was performed using the same level of theory in the presence of an electric field of various strengths. This results in the evaluation of geometrical changes in the presence of OEEFs. Furthermore, to account for the variation in energy on the optimised geometries, single-point calculations have been performed in the presence of OEEFs. Similar to the field-free method, the effect of solvation on the net energy has also been explored with THF using the SMD solvation model using the UB3LYP/def2-TZVPP methodology.

Recently, it has been shown that OEEFs could be applied experimentally using an STM gold tip. To mimic the experimental setup, we have designed a model system where a gold cluster is connected to the complex through a thiol linker $\{(O(CH_2CH_2)_2N)(CH_2)_3S\}$. The geometrical relaxation and binding energy calculations of complex **1** on the Au(111) surface were performed with periodic PBE/DZVP[70,71] setups using the CP2K suite.[72,73] A three-layer slab model with unit cell parameters $a = b = c = 2.94$ Å was included. For the Au216 and Au48 units, we have used 7 × 8 and 4 × 4 supercells, respectively, with 25 Å vacuum along the *Z*-direction. During the optimisation, we have relaxed the supercell fully, including molecules and the surface. The transition states were computed with only the Au5 unit model in the Gaussian suite using the Berny optimisation method. To exclude any undesirable interaction, the orientation of the Au_5 cluster was constrained, and thereafter, an OEEF was applied along the reaction axis (Fe–O bond) of the modelled cluster to investigate the effect of the electric field and gold cluster together. We have also explored a non-metallic surface, like graphene, to investigate a suitable surface candidate for the fabrication of a catalyst and, thereafter, the application of OEEFs. To understand the molecular stability of **1** on the graphene surface, we have performed periodic DFT optimisation in the CP2k suite using the PBE functional.[72]

Conflicts of interest

There are no conflicts to declare.

Data availability

All data supporting the findings of this study are available in the Supplementary Information (SI) associated with this manuscript. The coordinates of the DFT optimised molecules are given in a separate XYZ file. Supplementary information: DFT-optimised Cartesian coordinates for studied complexes, transition state diagrams, UV-visible plots, tables containing energetics of several spin states, natural charges, spin density plots, molecular orbital diagrams, and other data involved in this study. See DOI: **https://doi.org/10.1039/d5ta03554f**.

Acknowledgements

We thank DST and SERB (CRG/2018/00430; SB/SJF/2019-20/12) for funding. RKT and AS thank IITB for the IPDF fellowship.

References

1 A. Warshel, P. K. Sharma, M. Kato, Y. Xiang, H. Liu and M. H. Olsson, *Chem. Rev.*, 2006, **106**, 3210–3235.

2 H. Hirao, H. Chen, M. A. Carvajal, Y. Wang and S. Shaik, *J. Am. Chem. Soc.*, 2008, **130**, 3319–3327.

3 W. Lai, H. Chen, K.-B. Cho and S. Shaik, *J. Phys. Chem. Lett.*, 2010, **1**, 2082–2087.

4 S. P. de Visser, *Chem.–Eur. J.*, 2020, **26**, 5308–5327.

5 R. L. Shook and A. Borovik, *Inorg. Chem.*, 2010, **49**, 3646–3660.

6 W. Liu, P. J. Das, H. M. Colquhoun and J. F. Stoddart, *CCS Chem.*, 2022, **4**, 755–784.

7 R. Davydov, R. Razeghifard, S.-C. Im, L. Waskell and B. M. Hoffman, *Biochemistry*, 2008, **47**, 9661–9666.

8 D. Hamdane, C. Xia, S.-C. Im, H. Zhang, J.-J. P. Kim and L. Waskell, *J. Biol. Chem.*, 2009, **284**, 11374–11384.

9 D. Usharani, C. Zazza, W. Lai, M. Chourasia, L. Waskell and S. Shaik, *J. Am. Chem. Soc.*, 2012, **134**, 4053–4056.

10 D. Bím and A. N. Alexandrova, *ACS Catal.*, 2021, **11**, 6534–6546.

11 S. Yadav, S. Shaik, S. A. Siddiqui, S. Kalita and K. D. Dubey, *J. Chem. Inf. Model.*, 2022, **62**, 1025–1035.

12 P. Schyman, W. Lai, H. Chen, Y. Wang and S. Shaik, *J. Am. Chem. Soc.*, 2011, **133**, 7977–7984.

13 A. Saju, P. S. Gunasekera, P. Morgante, S. N. MacMillan, J. Autschbach and D. C. Lacy, *J. Am. Chem. Soc.*, 2023, **145**, 13384–13391.

14 S. Banerjee, R. K. Tiwari, P. Chakraborty, G. Rajaraman and S. P. Rath, *Inorg. Chem. Front.*, 2025, **12**, 2613–2626.

15 S. Sarkar, R. K. Tiwari, D. Samanta, T. Guchhait, E. C. Sañudo, G. Rajaraman and S. P. Rath, *Angew. Chem., Int. Ed.*, 2024, **63**, e202402344.

16 S. Sarkar, P. Sarkar, D. Samanta, S. K. Pati and S. P. Rath, *ACS Catal.*, 2022, **12**, 9589–9601.

17 A. C. Aragones, N. L. Haworth, N. Darwish, S. Ciampi, E. J. Mannix, G. G. Wallace, I. Diez-Perez and M. L. Coote, *Nature*, 2016, **531**, 88–91.

18 R. Ramanan, D. Danovich, D. Mandal and S. Shaik, *J. Am. Chem. Soc.*, 2018, **140**, 4354–4362.

19 S. R. Bell and J. T. Groves, *J. Am. Chem. Soc.*, 2009, **131**, 9640–9641.

20 H. Gao and J. T. Groves, *J. Am. Chem. Soc.*, 2017, **139**, 3938–3941.

21 T. Stuyver, R. Ramanan, D. Mallick and S. Shaik, *Angew. Chem.*, 2020, **132**, 7989–7994.
22 S. Shaik, *ACS Phys. Chem. Au*, 2024, **4**, 191–201.
23 S. Shaik, S. P. De Visser and D. Kumar, *J. Am. Chem. Soc.*, 2004, **126**, 11746–11749.
24 S. Shaik, D. Danovich, W. Wu and P. C. Hiberty, *Nat. Chem.*, 2009, **1**, 443–449.
25 G. Sini, P. Maitre, P. C. Hiberty and S. S. Shaik, *J. Mol. Struct.: THEOCHEM*, 1991, **229**, 163–188.
26 A. Sen and G. Rajaraman, *Inorg. Chem.*, 2023, **62**, 2342–2358.
27 J. Joy, T. Stuyver and S. Shaik, *J. Am. Chem. Soc.*, 2020, **142**, 3836–3850.
28 S. A. Siddiqui, T. Stuyver, S. Shaik and K. D. Dubey, *JACS Au*, 2023, **3**, 3259–3269.
29 A. Timmins, N. J. Fowler, J. Warwicker, G. D. Straganz and S. P. De Visser, *Front. Chem.*, 2018, **6**, 513.
30 M. A. Ehudin, L. B. Gee, S. Sabuncu, A. Braun, P. Moënne-Loccoz, B. Hedman, K. O. Hodgson, E. I. Solomon and K. D. Karlin, *J. Am. Chem. Soc.*, 2019, **141**, 5942–5960.
31 M. A. Ehudin, D. A. Quist and K. D. Karlin, *J. Am. Chem. Soc.*, 2019, **141**, 12558–12569.
32 R. Meir, H. Chen, W. Lai and S. Shaik, *ChemPhysChem*, 2010, **11**, 301–310.
33 Y. Luo, Y. Guan, G. Liu, Y. Wang, J. Li and L. Ricardez-Sandoval, *ACS Catal.*, 2024, **14**, 2696–2708.
34 A. Kausamo, J. Andersin and K. Honkala, *J. Phys. Chem. C*, 2014, **118**, 19759–19767.
35 X. Guo and S. Huang, *Electrochim. Acta*, 2018, **284**, 392–399.
36 Y. Luo, S. Cao, X. Du, Y. Wang and J. Li, *Mol. Catal.*, 2023, **535**, 112810.
37 R. Kumar, A. Ansari and G. Rajaraman, *Chem.–Eur. J.*, 2018, **24**, 6818–6827.
38 H. Hirao, D. Kumar, L. Que Jr and S. Shaik, *J. Am. Chem. Soc.*, 2006, **128**, 8590–8606.
39 W. Lai, H. Chen, S. Cohen and S. Shaik, *J. Phys. Chem. Lett.*, 2011, **2**, 2229–2235.
40 K. Keshari, M. Bera, L. Velasco, S. Munshi, G. Gupta, D. Moonshiram and S. Paria, *Chem. Sci.*, 2021, **12**, 4418–4424.
41 D. Schröder, S. Shaik and H. Schwarz, *Acc. Chem. Res.*, 2000, **33**, 139–145.
42 M. T. Green, J. H. Dawson and H. B. Gray, *Science*, 2004, **304**, 1653–1656.
43 D. Janardanan, Y. Wang, P. Schyman, L. Que Jr and S. Shaik, *Angew. Chem.*, 2010, **122**, 3414–3417.
44 T. Stuyver, J. Huang, D. Mallick, D. Danovich and S. Shaik, *J. Comput. Chem.*, 2020, **41**, 74–82.
45 S. Shaik, D. Danovich, J. Joy, Z. Wang and T. Stuyver, *J. Am. Chem. Soc.*, 2020, **142**, 12551–12562.
46 R. Nabi and G. Rajaraman, *Chem. Commun.*, 2019, **55**, 8238–8241.
47 J. I. Rodríguez, U. A. Vergara-Beltran and J. Autschbach, *Chem. Phys. Lett.*, 2019, **732**, 136625.
48 J. I. Rodríguez, E. A. Uribe, M. I. Baltazar-Méndez, J. Autschbach, F. Castillo-Alvarado and I. Gutiérrez-González, *Chem. Phys. Lett.*, 2016, **660**, 287–294.
49 X. Meng, J. Möller, M. Mansouri, D. Sánchez-Portal, A. Garcia-Lekue, A. Weismann, C. Li, R. Herges and R. Berndt, *ACS Nano*, 2022, **17**, 1268–1274.
50 R. K. Tiwari, R. Paul and G. Rajaraman, *Dalton Trans.*, 2024, **53**, 14623–14633.
51 R. Sánchez-de-Armas and C. J. Calzado, *Phys. Chem. Chem. Phys.*, 2023, **25**, 21673–21683.
52 S. Marocchi, A. Candini, D. Klar, W. Van den Heuvel, H. Huang, F. Troiani, V. Corradini, R. Biagi, V. De Renzi and S. Klyatskaya, *ACS Nano*, 2016, **10**, 9353–9360.
53 A. Candini, S. Klyatskaya, M. Ruben, W. Wernsdorfer and M. Affronte, *Nano Lett.*, 2011, **11**, 2634–2639.
54 A. S. Gajarushi, M. Wasim, R. Nabi, S. Kancharlapalli, V. R. Rao, G. Rajaraman, C. Subramaniam and M. Shanmugam, *Mater. Horiz.*, 2019, **6**, 743–750.
55 R. Nabi, R. K. Tiwari and G. Rajaraman, *Chem. Commun.*, 2021, **57**, 11350–11353.
56 S. Bhunia, A. Rana, S. G. Dey, A. Ivancich and A. Dey, *Chem. Sci.*, 2020, **11**, 2681–2695.
57 M. J. Frisch, G. W. Trucks, H. B. Schlegel, G. E. Scuseria, M. A. Robb, J. R. Cheeseman, G. Scalmani, V. Barone, G. A. Petersson, H. Nakatsuji, X. Li, M. Caricato, A. V. Marenich, J. Bloino, B. G. Janesko, R. Gomperts, B. Mennucci, H. P. Hratchian, J. V. Ortiz, A. F. Izmaylov, J. L. Sonnenberg, D. Williams-Young, F. Ding, F. Lipparini, F. Egidi, J. Goings, B. Peng, A. Petrone, T. Henderson, D. Ranasinghe, V. G. Zakrzewski, J. Gao, N. Rega, G. Zheng, W. Liang, M. Hada, M. Ehara, K. Toyota, R. Fukuda, J. Hasegawa, M. Ishida, T. Nakajima, Y. Honda, O. Kitao, H. Nakai, T. Vreven, K. Throssell, J. A. Montgomery Jr, J. E. Peralta, F. Ogliaro, M. J. Bearpark, J. J. Heyd, E. N. Brothers, K. N. Kudin, V. N. Staroverov, T. A. Keith, R. Kobayashi, J. Normand, K. Raghavachari, A. P. Rendell, J. C. Burant, S. S. Iyengar, J. Tomasi, M. Cossi, J. M. Millam, M. Klene, C. Adamo, R. Cammi, J. W. Ochterski, R. L. Martin, K. Morokuma, O. Farkas, J. B. Foresman and D. J. Fox, *Gaussian 16, Revision B.01*, Gaussian, Inc., Wallingford CT, 2016.
58 Y. Zhao and D. G. Truhlar, *J. Chem. Phys.*, 2006, **125**, 194101.
59 P. J. Hay and W. R. Wadt, *J. Chem. Phys.*, 1985, **82**, 270–283.
60 M. Radon, E. Broclawik and K. Pierloot, *J. Chem. Theory Comput.*, 2011, **7**, 898–908.
61 M. E. Ali, B. Sanyal and P. M. Oppeneer, *J. Phys. Chem. B*, 2012, **116**, 5849–5859.
62 J. P. Perdew, K. Burke and M. Ernzerhof, *Phys. Rev. Lett.*, 1996, **77**, 3865.
63 F. A. Hamprecht, A. J. Cohen, D. J. Tozer and N. C. Handy, *J. Chem. Phys.*, 1998, **109**, 6264–6271.
64 J. Tao, J. P. Perdew, V. N. Staroverov and G. E. Scuseria, *Phys. Rev. Lett.*, 2003, **91**, 146401.
65 O. Salomon, M. Reiher and B. A. Hess, *J. Chem. Phys.*, 2002, **117**, 4729–4737.
66 M. Reiher, O. Salomon and B. Artur Hess, *Theor. Chem. Acc.*, 2001, **107**, 48–55.
67 C. Adamo and V. Barone, *J. Chem. Phys.*, 1999, **110**, 6158–6170.

68 S. Grimme, *Wiley Interdiscip. Rev.: Comput. Mol. Sci.*, 2011, **1**, 211–228.

69 J. Zheng, X. Xu and D. G. Truhlar, *Theor. Chem. Acc.*, 2011, **128**, 295–305.

70 M. Ernzerhof and G. E. Scuseria, *J. Chem. Phys.*, 1999, **110**, 5029–5036.

71 A. C. Scheiner, J. Baker and J. W. Andzelm, *J. Comput. Chem.*, 1997, **18**, 775–795.

72 B. G. Lippert, J. H. Parrinello and Michele, *Mol. Phys.*, 1997, **92**, 477–488.

73 J. VandeVondele, M. Krack, F. Mohamed, M. Parrinello, T. Chassaing and J. Hutter, *Comput. Phys. Commun.*, 2005, **167**, 103–128.